

Supplementary material

Extreme drought–accelerated dissolved carbon metabolism triggers pulsed CO₂ outgassing in karst lakes

Maofei Ni¹, Weijun Luo², Junbing Pu³, Guangneng Zeng^{1*}, Jinxiao Long¹, Jia Chen², Jing Zhang³, Xiaodan Wang¹, Zhikang Wang^{1}**

1. College of Eco-Environmental Engineering, Guizhou Minzu University, Guiyang 550025, China.

2. State Key Laboratory of Environmental Geochemistry, Institute of Geochemistry, Chinese Academy of Sciences, Guiyang, 550081, China

3. Karst Research Team, Chongqing Key Laboratory of Carbon cycle and Carbon regulation of Mountain Ecosystem, School of Geography and Tourism, Chongqing Normal University, Chongqing, 401331, China

Number of pages: 18

Number of supporting texts: 3

Number of supporting figures: 9

Contents

Supplementary Text S1: Solid-phase extraction for FT-ICR MS

Supplementary Text S2: Lake areal CO₂ efflux calculation

Supplementary Text S3: Definition of latent variables in structural equation **model**

Fig. S1. *In-situ* measured atmospheric CO₂ equilibrium ($p\text{CO}_{2\text{air}}$) across periods.

Fig. S2. Uncertainty analysis of alkalinity-based DIC species calculation.

Fig. S3. Temporal patterns of DIC species (total DIC, HCO₃⁻, CO₃²⁻ and dissolved CO₂) in the karst lakes.

Fig. S4. Temporal patterns of fluorescent DOC abundance in the karst lakes.

Fig. S5. Comparison of ASV number in the karst waters across periods.

Fig. S6. Van Krevelen diagram showing Pearson's r of the dominant microorganisms with DOC molecular composition.

Fig. S7. Temporal shifts in fluorescence intensities of terrigenous and biogenic DOC extracted from PARAFAC modelling.

Fig. S8. Temporal shifts of statistical correlations between dissolved C and microbiome in the karst lakes.

Fig. S9. Van Krevelen diagram showing Pearson's r of DOC molecular composition with $p\text{CO}_2$ and CO₂ flux.

Supplementary Text S1: Solid-phase extraction for FT-ICR MS

The molecular composition of lake DOM was analyzed using FT-ICR MS (Bruker Solari X, Germany). Water samples were acidified to pH 2.0 with hydrochloric acid and filtered through a 200 mg PPL column (3 mL). The column was activated with 30 mL of methanol, and salts were removed using 30 mL of Milli-Q water and hydrochloric acid. The flow rate was maintained at 1–2 mL min⁻¹, with samples washed using 3 mL of HPLC-grade methanol. A negative electrospray ionization (ESI) source injected the samples into a Bruker Solarix XR 7.0T FT-ICR MS system at a flow rate of 120 µL h⁻¹, with injection and extraction voltages of 4.0 kV and -500 V for the capillary inlet. Mass-to-charge ratios (m/z) ranged from 100 to 1200, with an ion accumulation time of either 0.02 or 0.06 s. During FT-ICR MS analysis, $m/z = 369.119106$ served as the internal reference ion for real-time mass calibration. The procedure included acquiring 300 single transients/scans to enhance the signal-to-noise ratio (S/N) of target peaks. To ensure high-quality FT-ICR MS results, Suwannee River natural organic matter (SRNOM) was used as a calibration standard for the mass axis (Ni et al., 2024).

Supplementary Text S2: Lake areal CO₂ efflux calculation

The areal CO₂ flux (F, mmol/m²/d) from karst lakes was determined using the thin boundary layer model (Finlay et al., 2015) as follows:

$$\text{areal CO}_2 \text{ efflux} = k \times K_h \times (p\text{CO}_{2\text{water}} - p\text{CO}_{2\text{air}}) \quad (1)$$

$$K_h = 10^{-(1.11+0.016 \cdot T - 0.00007 \cdot T^2)} \quad (2)$$

Where k (cm/h) is the site-specific CO₂ gas transfer velocity, $p\text{CO}_{2\text{water}}$ (μatm) and $p\text{CO}_{2\text{air}}$ (μatm) are the aqueous and atmospheric CO₂ partial pressures, respectively. K_h (mmol/m³/μatm) is the temperature-corrected solubility coefficient (Henry's constant) for water temperature T (°C). k (cm/h) is the site-specific gas transfer velocity of CO₂.

Lake DIC species (H₂CO₂, HCO₃⁻, CO₃²⁻ and dissolved CO₂) and $p\text{CO}_2$ were calculated using the CO2SYS program (D.E. Pierrot et al., 2006), which determines carbonate equilibria based on total alkalinity, dissolved inorganic carbon (DIC), water temperature, and pH. The program is biased by the contributions from non-carbonate ion concentrations e.g., hydroxyl ([OH⁻]), hydrogen ion ([H⁺]), phosphate ([PO₄³⁻]), hydrogen phosphate [HPO₄²⁻], borate ([B(OH)₄⁻]), ammonia ([NH₃]), silicate ([SiO(OH)₃⁻]), hydrofluoric acid ([HF]), hydrogen sulfate ([HSO₄⁻]) and phosphoric acid ([H₂SO₄]), and particularly, organic acids. Under atmospheric pressures, the CO₂ fugacity ($f\text{CO}_2$) was approximately 0.3% lower than $p\text{CO}_2$, reflecting the non-ideality of CO₂ as a function of DIC, pH and water temperature (Equation 3-4).

$$\begin{aligned} TA = & [\text{HCO}_3^-] + 2[\text{CO}_3^{2-}] + [\text{OH}^-] - [\text{H}^+] + [\text{B(OH)}_4^-] + [\text{HPO}_4^{2-}] + 2[\text{PO}_4^{3-}] \\ & + [\text{SiO(OH)}_3^-] + [\text{NH}_3] - [\text{HSO}_4^-] - [\text{H}_3\text{PO}_4] - [\text{HF}] \quad (3) \end{aligned}$$

$$fCO_2 = \frac{DIC}{K_0} \times \frac{[H^+]^2}{[H^+]^2 + K_1 \times [H^+] + K_1 \times K_2} \quad (4)$$

$$pK_0 = -7 \times 10^{-5}T^2 + 0.016T + 1.11 \quad (5)$$

$$pK_1 = 1.1 \times 10^{-4}T^2 - 0.012T + 6.58 \quad (6)$$

$$pK_2 = 9 \times 10^{-5}T^2 - 0.0137T + 10.62 \quad (7)$$

where $pK = -\lg K$. K_0 , K_1 and K_2 represent the solubility coefficient of CO_2 , first and second dissociation constants, respectively. These constants are temperature-dependent and determined using Henry's Law for freshwater, as outlined in Equations (5), (6) and (7).

Lake k is dominated by wind speed and can be modelled using the following empirical equations:

$$k_T = k_{600} \left(\frac{S_{CT}}{600} \right)^{-2/3} \quad (8)$$

$$S_{CT} = 1911.1 - 118.11T + 3.4527T^2 - 0.04132T^3 \quad (9)$$

$$k_{600} = 2.07 + 0.215U_{10}^{1.7} \quad (U_{10} < 3.0 \text{ m s}^{-1}) \quad (10)$$

$$k_{600} = 0.45U_{10}^{1.64} \quad (3.0 < U_{10} < 5.0 \text{ m s}^{-1}) \quad (11)$$

$$U_{10} = U_z \left[1 + \frac{(C_{d10})^{1/2}}{Kc} \times \ln\left(\frac{10}{z}\right) \right] \quad (12)$$

where k_T (cm/h) represents the k value at a temperature of T , while S_{CT} is the Schmidt number (dimensionless) corrected using T . k_{600} (cm/h) denotes the normalized gas transfer velocity of CO_2 . The empirical equations vary based on U_{10} (wind speed at 10 m above water, in m/s), converted using the logarithmic wind profile relationship (Equation 12). Here, z is the wind speed measurement height, C_{d10} is the drag coefficient at 10 m (0.0013 m/s), and Kc is the von Karman constant (0.41).

Supplementary Text S3: Definition of latent variables in structural equation model

In our structural equation model, we established six latent variables (with observed variables): 1) microbial community (top 5 high-abundance microorganisms), 2) DIC species (DIC, HCO_3^- , CO_3^{2-} and dissolved CO_2), 3) UV-vis DOC properties (DOC, SUVA_{254} and $\text{S}_{275-295}$), 4) fluorescent DOC composition (PARAFAC C1 and C2), 5) fluorescent DOC properties (FI, BIX and HIX), and 6) CO_2 flux (CO_2 evasion rate). These latent variables were further specifically defined according to the loadings of their associated observed variables, shown in Fig. SI-1.

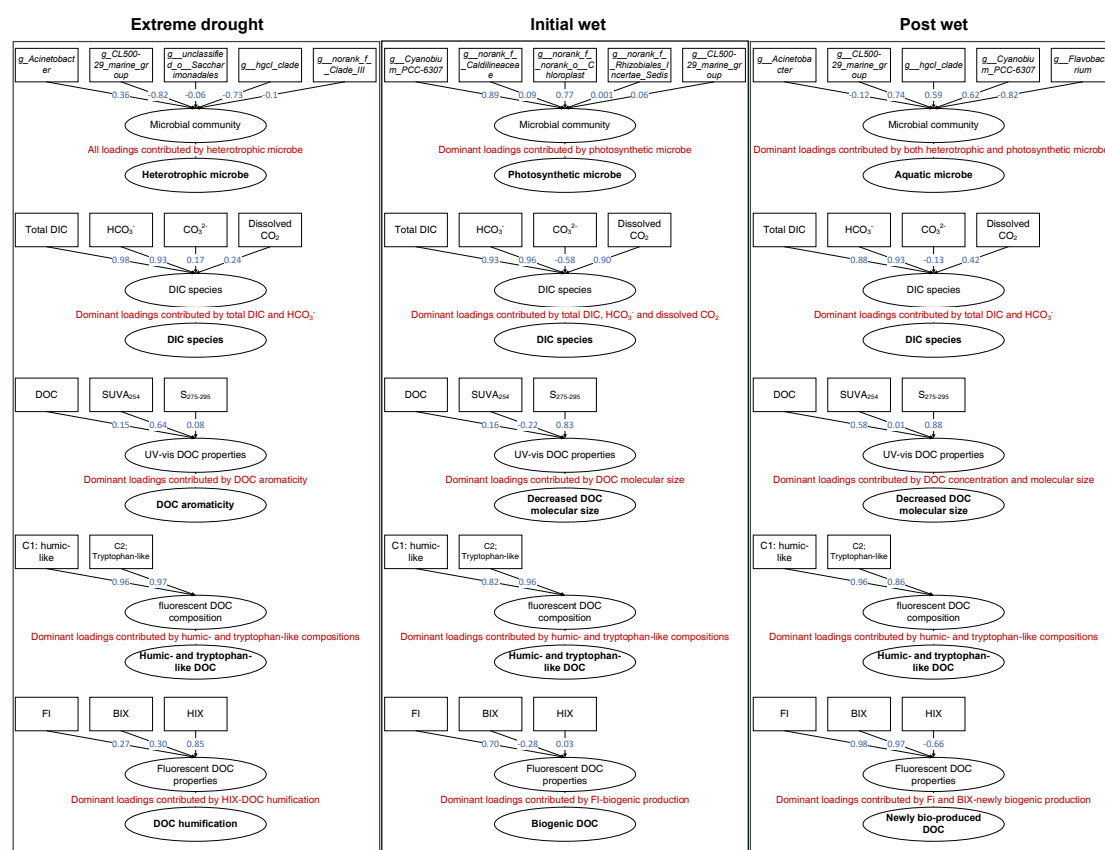


Fig. ST-1. Define and specify latent variables from the loadings of observed variables in structural equation model. Rectangles and ellipses represent observed variables and latent variables, respectively. The arrow labels indicate the corresponding loadings.

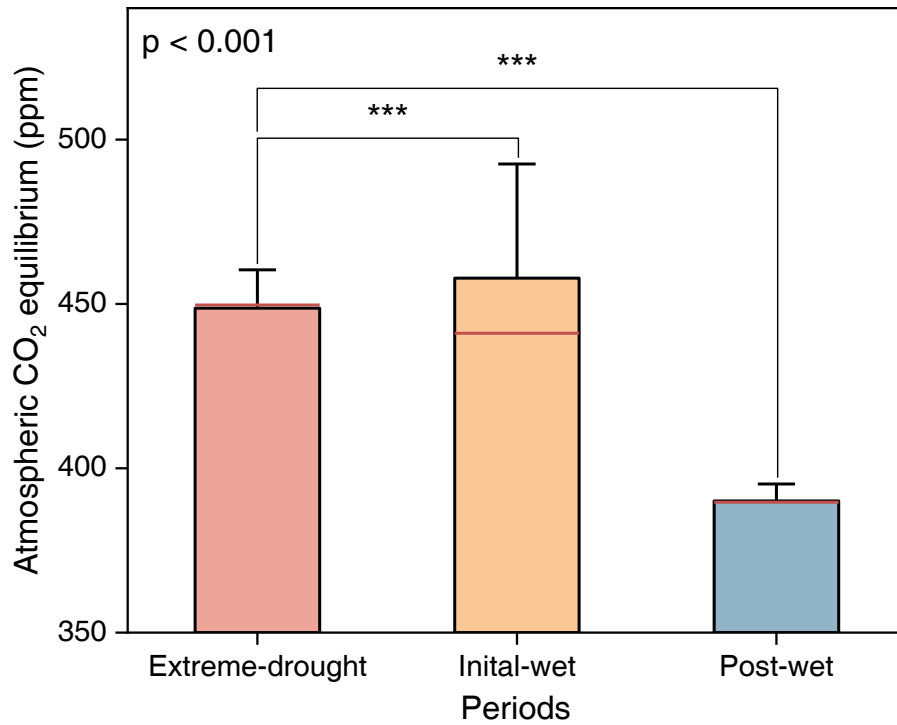


Fig. S1. *In-situ* measured atmospheric CO₂ equilibrium ($p\text{CO}_{2\text{air}}$) across periods. The box with whisker shows mean with standard deviation. The red line represents median value. We found significant higher atmospheric CO₂ concentrations in the extreme-drought (449 ± 8 ppm) and initial-wet periods (458 ± 30 ppm) in comparison to post-wet period (390 ± 5 ppm) ($p < 0.001$). These air backgrounds encompass global average CO₂ measurements in 2022 and 2023 (<https://gml.noaa.gov/ccgg/trends/>), which were adjusted to μatm units for estimating areal CO₂ efflux using a thin boundary layer model.

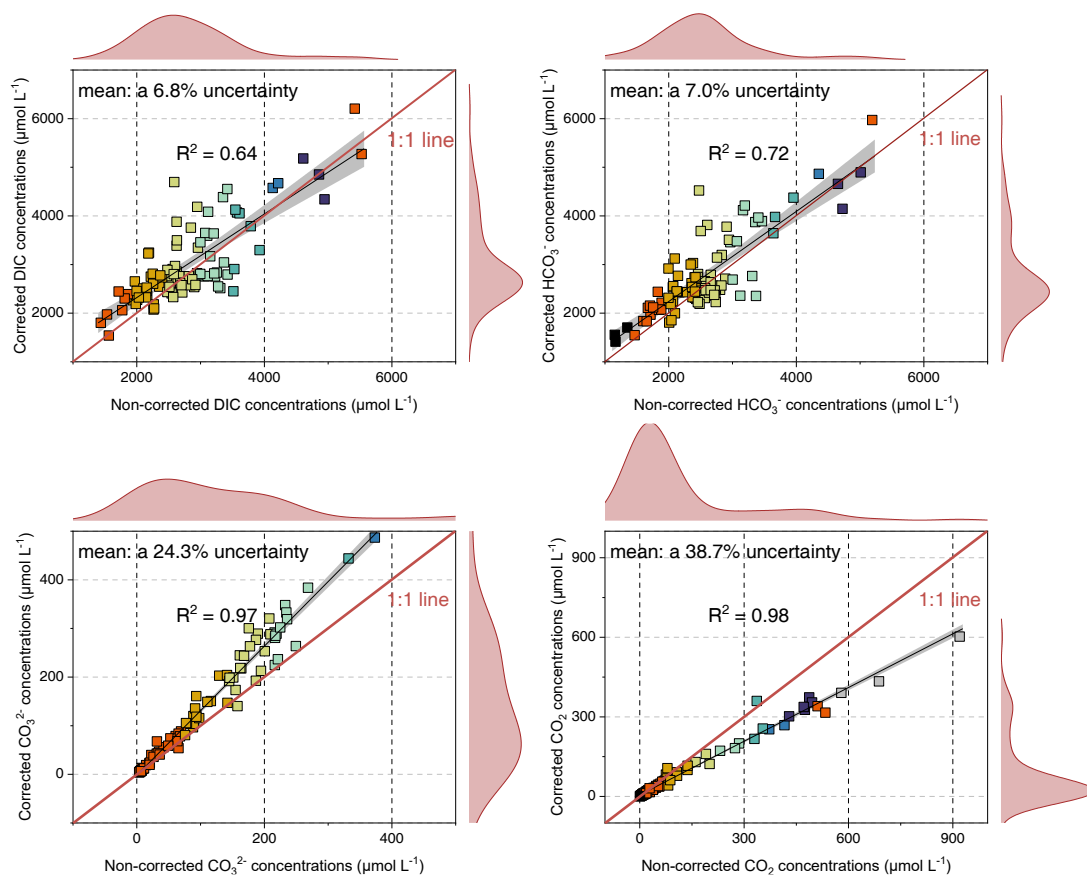


Fig. S2. Uncertainty analysis of alkalinity-based DIC species calculation. We found that corrected and non-corrected DIC species were highly associated in carbonate equilibria program. The uncertainties of total DIC (6.8%) and HCO₃⁻ (7.0%) are relatively small, suggesting low contributions from non-carbonate alkalinity in the karst waters. In contrast, we show extremely high correlations between corrected and non-corrected CO₃²⁻/dissolved CO₂ ($R^2 > 0.95$) with large uncertainties. Specifically, averaged CO₃²⁻ was underestimated by 24.3%, while averaged dissolved CO₂ was overestimated by 38.7%. This suggests that small variations in non-carbonate alkalinity can result in large uncertainties of low-level DIC terms, especially the case for CO₂ concentrations and thus CO₂ emissions from aquatic environments.

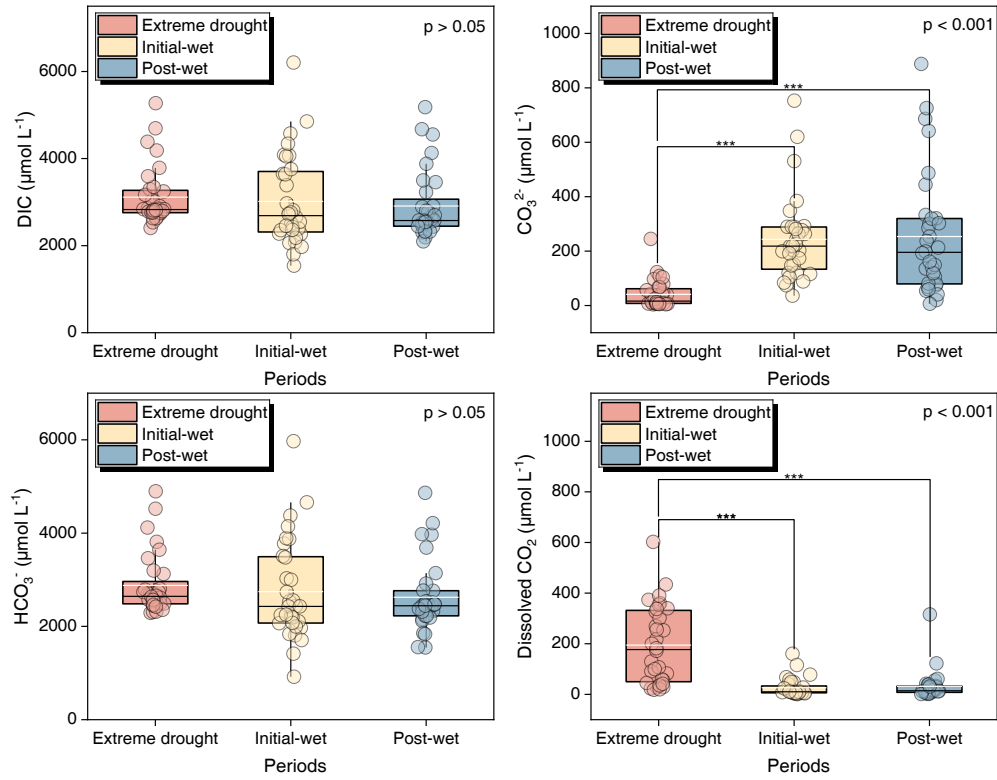


Fig. S3. Temporal patterns of DIC species (total DIC, HCO_3^- , CO_3^{2-} and dissolved CO_2) in the karst lakes. The box with scatters shows 5th–95th percentiles with all data. The black and white lines show median and mean, respectively. We found that extreme droughts caused lower CO_3^{2-} but higher dissolved CO_2 concentrations in comparison to wet conditions ($p < 0.001$).

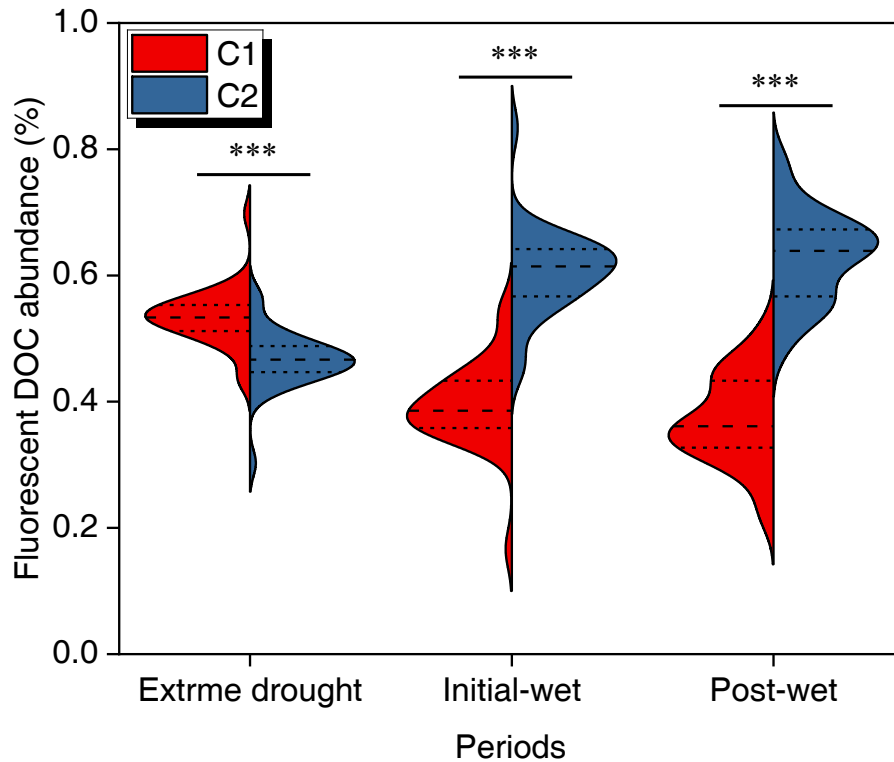


Fig. S4. Temporal patterns of fluorescent DOC abundance in the karst lakes. The half violin shows maximum fluorescence intensity proportions of humic-like (C1) and tryptophan-like DOC (C2), depicted through a Kernel Smooth distribution. We suggest that %C1 and %C2 were significantly different across periods, particularly with %C1 > %C2 during extreme droughts yet %C1 < %C2 during wet conditions ($p < 0.001$). This implies a metabolic shift from catabolism to anabolism in aquatic environments, characterized by changes in tryptophan-like DOC from consumption during extreme drought to accumulation during wet periods.

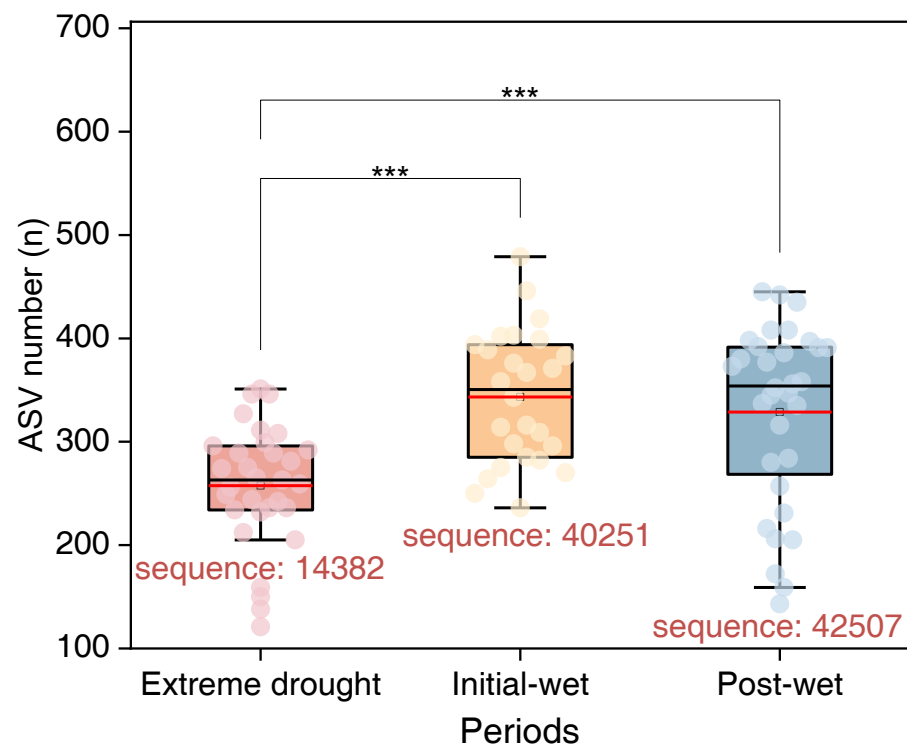


Fig. S5. Comparison of ASV number in the karst waters across periods. The box with scatters shows 5th–95th percentiles with all data. The black and red lines show median and mean, respectively. It shows that the extreme drought greatly reduced ASV number (and sequence number) in comparison to wet periods ($p < 0.001$).

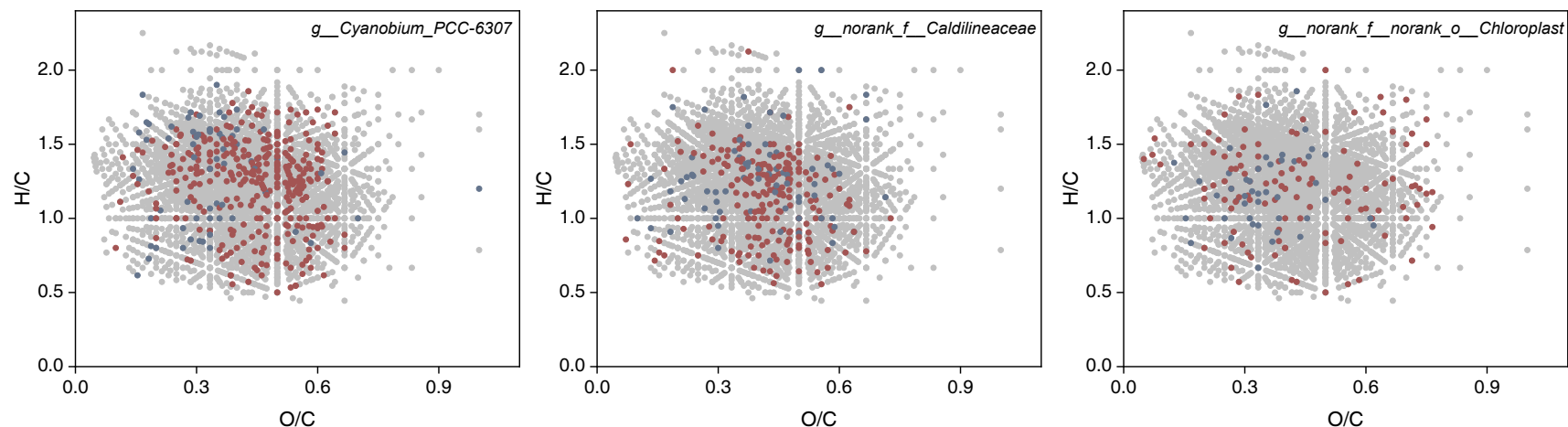


Fig. S6. Van Krevelen diagram showing Pearson's r of the dominant microorganisms with DOC molecular composition. Dots in red, blue and grey represent positive ($p < 0.05$), negative ($p < 0.05$), and no statistical correlations ($p > 0.05$), respectively. The specific molecular formula is not shown in this figure, and we thus upload the dataset as Supplement table S1. We show that as microbial abundance declines, fewer molecules show significant correlations with microorganisms. Specifically, photosynthetic microorganisms proliferate significantly, showing positive associations with lipid-like and carbohydrate compounds, and negative associations with polyhydroxy substances. In contrast, heterotrophic microorganisms show positive associations with N-containing aromatics and polyhydroxy substances, and negative associations with S-

containing aromatics and high-molecular-weight humic substances. Therefore, we know that in karst lakes, 1) phototrophic metabolism increases both carbohydrate and lipid-like compound abundance: photosynthesis generates substantial quantities of biodegradable DOC; 2) N-containing aromatics and polyhydroxy substances fuel heterotrophic microorganisms; 3) S-containing aromatics and high-molecular-weight humic substances are refractory organic C for the karst aquatic microorganisms.

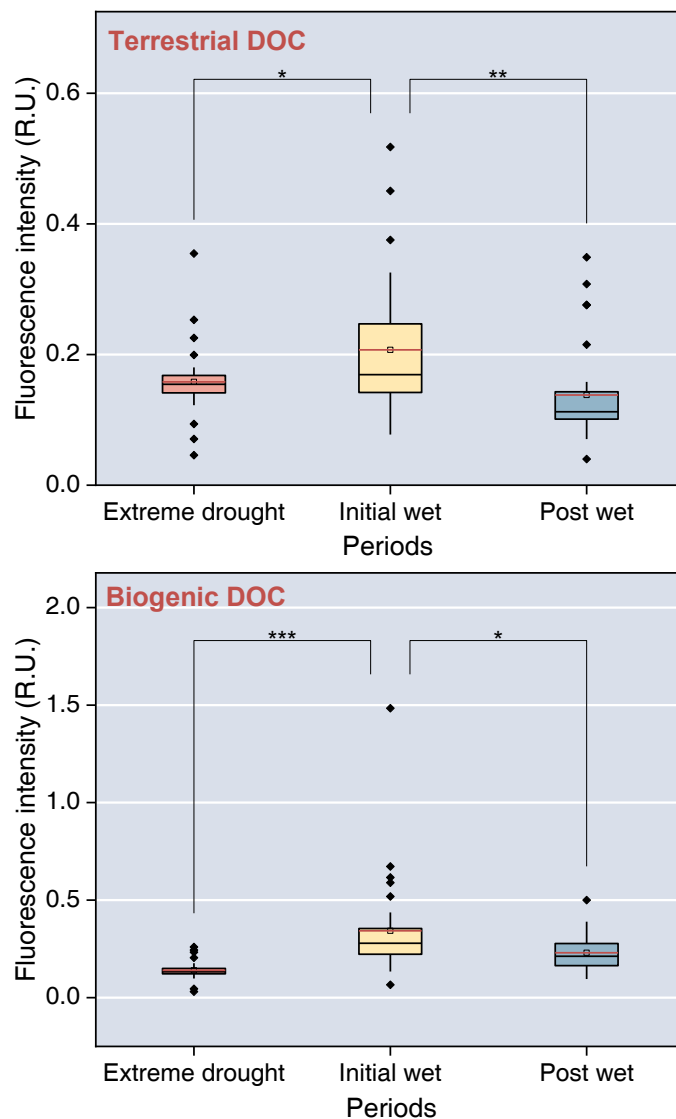


Fig. S7. Temporal shifts in fluorescence intensities of terrigenous and biogenic DOC extracted from PARAFAC modelling. The box with scatters shows 25th–75th percentiles with outliers. The black and red lines show median and mean, respectively. We show that the initial wet condition substantially increases terrigenous and biogenic DOC inputs ($p < 0.05$). This happened following the end of extreme droughts as a result of more abundant rainfall. We therefore suggest that rainfall events following extreme droughts likely amplify both terrestrial inputs and biological revival within aquatic ecosystems.

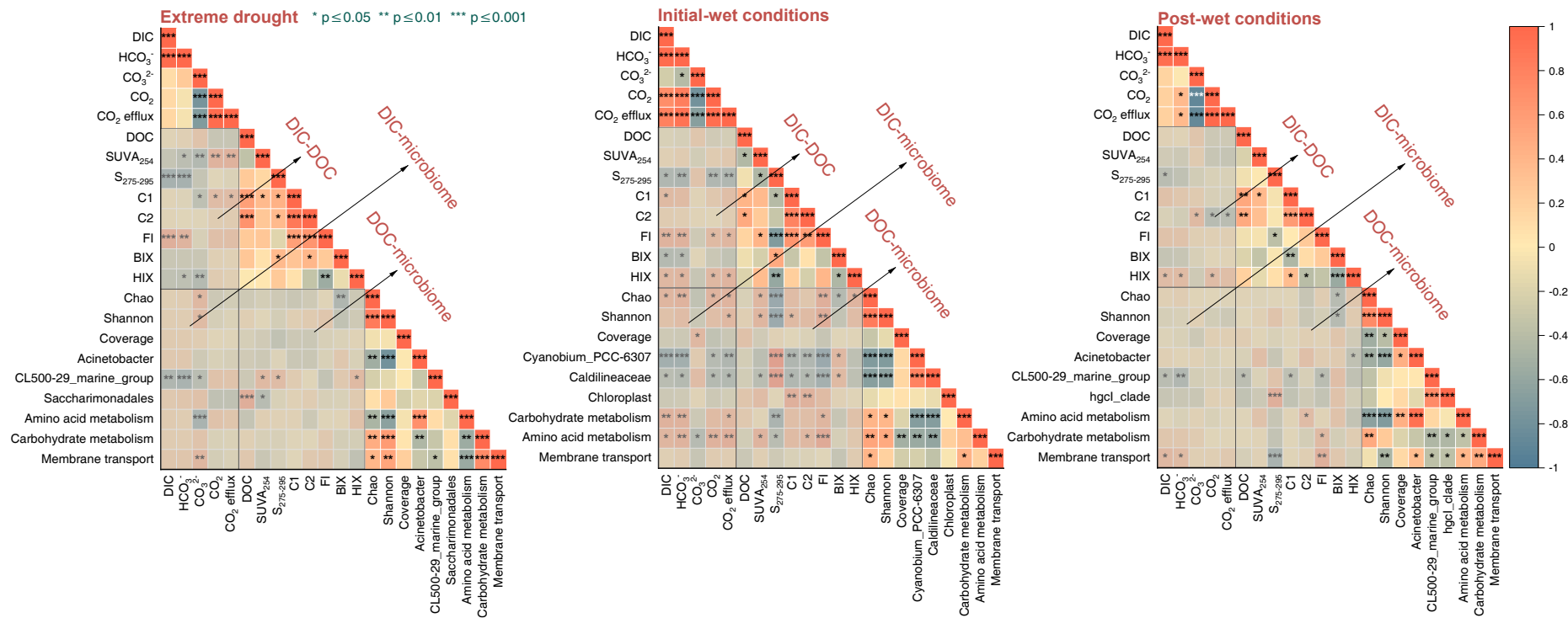


Fig. S8. Temporal shifts of statistical correlations between dissolved C and microbiome in the karst lakes. The relationships between DIC, DOC and microbiome are highly variable at timescales. Apparently, these correlations were prevalent during initial-wet period (summer), indicating diverse pathways established through aquatic photosynthesis, respiration and terrestrial inputs. Extreme drought and post-wet conditions, however, can decouple partial linkages of dissolved C with microbiome. This is attributable to the facts that 1) turnover paths are relatively

limited due to depleted active C, or alternatively 2) statistical correlations among variables are mutually interfering. Specifically, **1) extreme-drought period:** Lake CO₂ and CO₂ emissions linked to the increased aromaticity (SUVA₂₅₄) and humic-like component (C1), attributable to exhausted labile DOC and accumulated recalcitrant DOC (see DIC-DOC section). *CL500-29_marine_group* is responsible for increased aromaticity and humification (HIX) due to respiratory metabolism (see DOC-microbiome section). **2) initial-wet period:** We show that photosynthesis stimulates biological production of low-molecular-weight DOM (FI and S₂₇₅₋₂₉₅, see DIC-DOC section), while photosynthesis-related *Cyanobium_PCC-6307* consumes DIC, HCO₃⁻ and CO₂ (see DIC-microbiome section). This directly demonstrates that karst lake CO₂ allocation is primarily driven by photosynthetic uptake of DIC species during initial-wet period (summer). **3) post-wet period:** Tryptophan-like DOC metabolism primarily fuels lake CO₂ (see DIC-DOC section). Therefore, we suggest that photosynthetically generated DOC e.g., carbohydrates can be quickly metabolized, and CO₂ contributors are greatly reduced during post-wet period. From this perspective, we highlight that C sink from photosynthetic CO₂ uptake primarily occurs during initial-wet period (summer) in karst lakes.

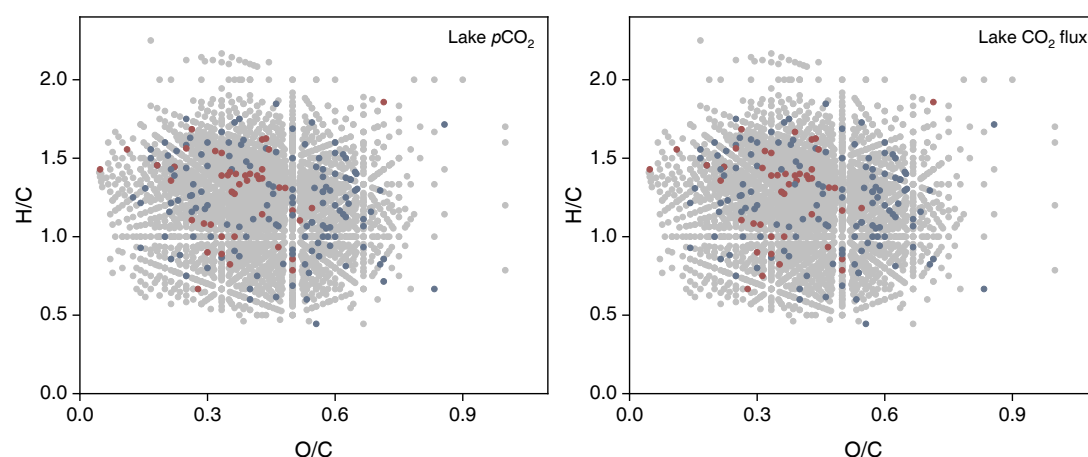


Fig. S9. Van Krevelen diagram showing Pearson's r of DOC molecular composition with $p\text{CO}_2$ and CO_2 flux. Dots in red, blue and grey represent positive ($p < 0.05$), negative ($p < 0.05$), and no statistical correlations ($p > 0.05$), respectively. The specific molecular formula is not shown in this figure, and we thus upload the dataset as Supplement table S1. We found that $p\text{CO}_2$ and CO_2 flux show consistent correlations with DOC molecular composition. Specifically, lake CO_2 correlates positively with polymer by-products and humic compounds, but negatively with amino acids, aliphatic compounds and small molecular organic acids. This suggests that in karst lakes: 1) amino acids, aliphatic compounds and small molecular organic acids serve as primary substrates driving CO_2 production and emissions; 2) relative accumulation of high-molecular-weight recalcitrant polymer by-products and humic compounds may be indicative of CO_2 emission potential.

References

- D.E. Pierrot, D.W.R. Wallace, and E. Lewis: MS Excel Program Developed for CO₂ System Calculations, ORNL/CDIAC-105a. Carbon Dioxide Information Analysis Center, Oak Ridge National Laboratory, U.S. Department of Energy, Oak Ridge, Tennessee, doi: 10.3334/CDIAC/otg.CO2SYS_XLS_CDIAC105a, 2006. 2006.
- Finlay, K., Vogt, R. J., Bogard, M. J., Wissel, B., Tutolo, B. M., Simpson, G. L., and Leavitt, P. R.: Decrease in CO₂ efflux from northern hardwater lakes with increasing atmospheric warming, *Nature*, 519, 215-218, 2015.
- Ni, M., Liu, R., Luo, W., Pu, J., Wu, S., Wang, Z., Zhang, J., Wang, X., and Ma, Y.: A comprehensive conceptual framework for signaling in-lake CO₂ through dissolved organic matter, *Water Research*, 264, 122228, 2024.